SCIENTIFIC REPORTS

Mapping biological composition through quantitative phase and absorption X-ray ptychography

Michael W. M. Jones[1]*, Kirstin Elgass[2]†, Mark D. Junker[1], Mac B. Luu[1]‡, Michael T. Ryan[2]§, Andrew G. Peele[1,3,4] & Grant A. van Riessen[1]

[1]ARC Centre of Excellence for Coherent X-Ray Science, Department of Physics, La Trobe University, Bundoora 3086, Australia, [2]ARC Centre of Excellence for Coherent X-Ray Science, Department of Biochemistry, La Trobe University, Bundoora 3086, Australia, [3]Australian Synchrotron, 800 Blackburn Rd, Clayton 3168, Australia, [4]ARC Centre of Excellence for Advanced Molecular Imaging, Australian Synchrotron, 800 Blackburn Rd, Clayton 3168, Australia.

Isolating compositional information in biological X-ray imaging can be problematic as such information is conflated with thickness and density variations when viewing in projection through a sample. We demonstrate an effective method for identifying variations in material composition by simultaneously using the quantitative phase and magnitude images provided through soft X-ray ptychography. Using this approach we show significantly increased contrast and improved reliability of the identification of intracellular features from uncharacterised samples. While demonstrated for X-ray ptychography, this method is immediately applicable to electron and optical microscopy methods where the complex transmission function of the sample is recovered.

Quantitative microscopy methods in biological imaging enhance the information that may be obtained about the sample, and in particular, the intracellular features[1]. However, this information is a combination of the composition, thickness, and density, making it hard to separate these individual factors without significant *a priori* knowledge[1,2]. One method for obtaining quantitative biological images is X-ray Coherent Diffractive Imaging (CDI)[2–8], which can be used to image intracellular features with spatial resolution beyond the limits imposed by image-forming optics[9]. So called X-ray CDI ptychography[10] and phase-diverse[11,12] methods extend CDI by using overlapping information from multiple measurements of the sample to reduce artefacts and increase the robustness of the solution. Ptychography has also been demonstrated in optical[13] and electron microscopy[14,15], and therefore the following discussion applies equally to those regimes, as well as other microscopy methods where the complex transmission function of the sample is recovered[16].

Direct quantitative information has been successfully used in CDI to accurately measure the thickness, density, or elemental distribution of a characterised sample in two dimensions[2,17,18], and assist tomographic segmentation by isolating intracellular organelles[7]. However, it has typically been used more qualitatively in obtaining information as to the materials present from an uncharacterised sample in projection[19]. The direct quantitative information obtained from CDI is in the form of the phase and magnitude of the complex transmission function through the sample, which are, respectively, a function of the real and imaginary components of the energy dependent complex scattering factor, $\tilde{f} = f_1 + if_2$[20], and, jointly, of the density and thickness of the sample. For a projection through a sample of uniform density, the ratio of the phase and magnitude of the complex transmission function can be defined as a scattering quotient, f_q, which is a function only of the components of the scattering factor;

$$f_q = \frac{\ln(|T|)}{\phi} = \frac{\bar{f}_2}{\bar{f}_1} \qquad (1)$$

where $\bar{f}_2$ and $\bar{f}_1$ are the average of f_2 and f_1 along the projection through the sample, corresponding to the average of the materials present in the projection. When the phase and magnitude of the complex transmission function are reconstructed in three dimensions then, for small enough voxels, a single material will dominate and the scattering quotient can be calculated in each voxel as f_2/f_1. Further details regarding the application of the scattering quotient for specific cases are presented in the Supplementary Information. Consideration of f_1 and f_2 reveals that this method is particularly applicable to imaging biological material in the water-window, where

1
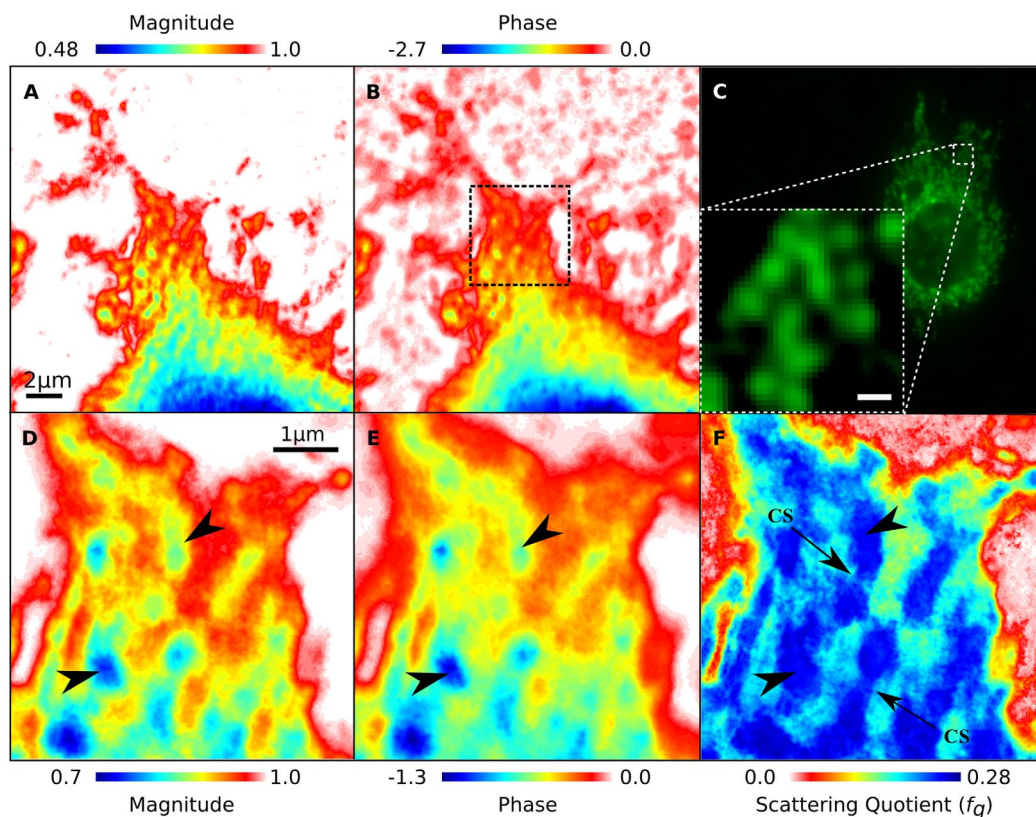
Figure 1 | The magnitude and phase of the reconstructed complex transmission function of a MEF cell are shown in panels A and B respectively. Panel C shows a fluorescent image of a MEF cell transfected with the fluorescent mitochondrial tag mito-Dendra2[26], with the inset view showing an enlarged area illustrating the mitochondrial morphology. Panels D, E, and F, show an enlarged region representing the inner box in Panel B and show the magnitude, phase retardation, and scattering quotient respectively. Arrowheads indicate the protein rich mitochondria, which appear as having the same composition as determined by the scattering quotient (F) with a similar morphology to those shown in Panel C. However, the same areas have inconsistent phase or magnitude values, Panels D and E, due to the variation in sample thickness and density, obscuring reliable identification. Arrows in (F) reveal constriction sites (CS) where mitochondrial fission events can occur, which cannot be otherwise identified. The scale bar in A is equal to 2 μm and the scale bars in C (inset), and D are equal 1 μm.

absorption contrast for carbon is much greater than for water. For example, in the water-window at an X-ray energy of 517 eV, the scattering quotient for empirical protein[21] ($C_{30}H_{50}N_9O_{10}S$) is equal to 0.26, for lipids with various concentrations of C, H, O, N, and P it ranges from 0.16 to 0.22, while for water it is equal to 0.04.

By creating a two-dimensional map of the scattering quotient projected through a sample we therefore expect to see a map that highlights compositional variations along each projection. We demonstrate here that, even though the uniform density assumption is not strictly valid, any density variations are sufficiently small that use of the scattering quotient creates sufficient contrast to enhance segmentation of features of a cell in projection based on their material differences. We apply this method to the identification of mitochondrial constriction sites in Mouse Embryonic Fibroblasts (MEFs).

Results and discussion

CDI data was collected at the Soft X-ray Imaging (SXRI) branchline of the Australian Synchrotron[22,23] at an X-ray energy in the water-window of 517 eV in order to identify the mitochondrial constriction sites in MEFs. Mitochondria are relatively small, isolated protein rich regions compared to the surrounding cytoplasm. However, in many cells, including cultured MEFs, there are large variations in cell thickness from the centre to the edges, obscuring the identification of protein rich mitochondria. These attributes of the MEF cell can readily be seen in both the reconstructed magnitude and phase of the complex transmission function for an area of the sample as shown in Figs. 1A and 1B respectively. The nucleus is clearly iden-

tified at the lower edge of the images as the thickest and most dense part of the cell, and, correspondingly, has the largest absorption and phase retardation. The cell extends towards the top of the image as it spreads over the substrate and becomes thinner. In the regions beyond the extent of the cell, amalgamations of Poly-L-lysine are observed as small dots[24]. In the thicker regions of the sample, we expect the mitochondria to be overlapping and therefore indistinct. However, in the thinner regions of the sample less overlap between different components with different composition is expected, and we therefore expect to be able to isolate mitochondrion through the scattering quotient map.

Enlarged views of the thinner region (inner box in Fig. 1B) are presented in Figs. 1D-1F corresponding to the reconstructed magnitude and phase of the complex transmission function, and the scattering quotient map respectively. It is immediately obvious that the scattering quotient map contains different and complementary information to the other images. Distinct organelles can be seen, and are consistently identifiable despite the changes in thickness observed in Figs. 1D, 1E, as expected. The most protein rich components of MEF cells are the nucleus and mitochondria. As Figs. 1D–1F represent an area that does not contain the nucleus, the most protein rich organelles in the cell are therefore most likely mitochondria. These can clearly be identified in Fig. 1F (arrowheads), showing a similar morphology and distribution to the fluorescence image presented in Fig. 1C. Further, mitochondrial constriction sites (CS) where fission events can occur[25] are identified with arrows. In the magnitude and phase images arrowheads indicate mitochondria
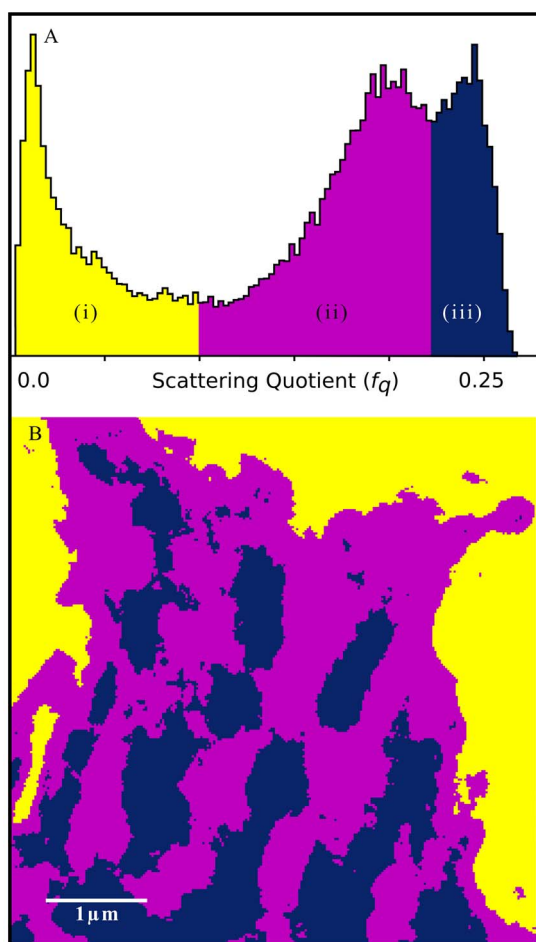
Figure 2 | Histogram of the values of the scattering quotient presented in Fig. 1F (A) with the scattering quotient map originally presented in Fig. 1F (B) segmented to represent the three regions found in the histogram. The mitochondria identified in Fig. 2 are obviously apparent, as is the extent of the cell. The scale bar in (B) is equal to 1 μm.

identified in Fig. 1F. However, the compositional information in the magnitude and phase images is obscured by variations in the sample thickness and density, making accurate identification unreliable.

To validate the assertion that different materials can be segmented based on the scattering quotient map, Fig. 1F, a histogram of the values contained in the image was generated. This histogram is presented in Fig. 2A, and clearly shows three major areas, corresponding to the protein rich mitochondria (iii), the cytoplasm (ii), made up of a mixture of various substances containing significantly less protein and more residual water than the mitochondria, and the background (i) corresponding to residual water. Each area is peaked at a value close to the expected value for the nominal material and has a distribution due to variations in the material, thickness, and the density along the particular projection. It can be seen that any variations have sufficiently small effect that a segmentation based on objectively resolving the three areas using the minimum in the histogram distribution provides a clear distinction between the features in the cell. That distinction is shown in Fig. 2B and clearly corresponds to the features identified in Fig. 1F.

Additional examples applying the method to a second MEF and a malaria infected red blood cell at the gametocyte life cycle stage are presented in Supplementary Figs. S1 and S2 respectively. In these examples, the information contained in the scattering quotient maps allows areas with different compositions to be isolated from each other. For the case in Fig. S1, the results mirror those presented in Figs 1 and 2, while for Fig S2, regions of the sample containing

haemoglobin and hemozoin are isolated from the surrounding regions using the scattering quotient alone.

The method presented in this paper takes advantage of the direct quantitative information provided in the recovered complex transmission function to effectively reduce the effect of variations in the sample thickness and density. This significantly increases the contrast, and makes it possible to isolate intracellular organelles in two-dimensional imaging. We apply the method to MEF cells, and use the information to reveal possible mitochondrial constriction sites which are otherwise unable to be identified in two-dimensional X-ray imaging. In some cases this may be used in lieu of three-dimensional imaging, but will also be able to be applied to three-dimensional imaging. In three dimensions, the scattering quotient is calculated voxel-wise from the three-dimensional complex transmission function across the entire specimen, eliminating the need for a valid projected scattering quotient to be calculated. This will allow segmentation by composition only, independent of density. We have demonstrated a method for image segmentation based on the sample composition that is robust to density and thickness variations, overcoming a key limitation of quantitative biological X-ray imaging.

Methods

Sample preparation. Mouse Embryonic Fibroblasts (MEFs) were cultured in complete DMEM with 10% fetal calf serum at 37 degrees and 5% CO_2. The cells were then trypsinized and resuspended, before 20 μl of the cell suspension was deposited on silicon nitride windows, which were previously coated with Poly-L-lysine (Sigma) for 2 h at 80 degrees and dried overnight. The cells were then put in the incubator for 4 h to allow the cells attach to the window. Fresh DMEM (10 μl) was added every 30 min to prevent cells from drying out. Once the cells had attached to the windows, they were fixed with 2.5% glutaraldehyde and freeze-dried overnight before imaging.

For fluorescence imaging, cells were transfected with mito-Dendra2[26] prior to transfer onto silicon nitride windows using Lipofectamine LTX (Life Technologies) according to the manufacturer's instructions. Cells were then fixed with 2% para-formaldehyde and 0.2% glutaraldehyde and imaged in phosphate buffered saline. Fluorescence images were recorded with a fluorescence microscope (IX81; Olympus) using a 40× air objective. Images were acquired using an F-view 2 camera (Olympus) and processed using Soft System SIS (Olympus).

X-ray data collection and analysis. X-ray data were collected using a 517 eV X-ray beam at the Soft X-ray Imaging (SXRI) branchline at the Australian Synchrotron[22] focused with a 160 μm diameter Fresnel zone plate (FZP) with an outer zone width of 30 nm. The combination of a 30 μm beamstop and 10 μm order sorting aperture (OSA) allowed only the first order focus of the FZP to propagate to the sample. A cooled charge-coupled device (CCD) detector (Princeton MT-MTE) with 2048 × 2048 square pixels each with a 13.5 μm side length was placed 25 cm downstream of the FZP. Under this experimental arrangement the theoretical resolution limit due to the numerical aperture (NA) of the detector is equal to 21 nm.

Diffraction data was collected over three 4 × 5 two-dimensional raster scans at three defocused distances, defined here as the distance from the focal point of the FZP to the sample, between 300 μm and 350 μm. The minimum lateral overlap fraction[11] for each two-dimensional raster scan was equal to 87%. A single exposure of 0.3 s was taken at each data collection point[12] resulting in a total imaging time of 18 s. We calculate the total dose received as less than 6.9×10^7 Gy assuming average composition of the sample is close to model protein[19,21]. The data were treated according to the method described in Ref. 27, before the complex transmission function was obtained using the phase-diverse CDI reconstruction functions[11] with a complex constraint[19] in the NADIA software library (http://cxscode.ph.unimelb.edu.au).

The resolution of the phase, magnitude, and scattering quotient maps was estimated from the power spectrum density (PSD) of the images to be approximately 30 nm.

1. Hanssen, E. *et al.* Soft X-ray microscopy analysis of cell volume and hemoglobin content in erythrocytes infected with asexual and sexual stages of *Plasmodium falciparum*. *J. Struct. Biol.* **177**, 224–232 (2012).
2. Jones, M. W. M. *et al.* Phase-diverse Fresel coherent diffractive imaging of malaria infected red blood cells in the water window. *Opt. Express* **21**, 32151–32159 (2013).
3. Dierolf, M. *et al.* Ptychographic X-ray computed tomography at the nanoscale. *Nature* **467**, 436–439 (2010).
4. Jiang, H. *et al.* Quantitative 3D imaging of whole, unstained cells by using X-ray diffraction microscopy. *Proc Natl Acad Sci USA* **107**, 11234–11239 (2010).
5. Giewekemeyer, K. *et al.* Quantitative biological imaging by ptychographic x-ray diffraction microscopy. *Proc Natl Acad Sci USA* **107**, 529–534 (2010).
6. Maiden, A. M., Morrison, G. R., Kaulich, B., Gianoncelli, A. & Rodenburg, J. M. Soft X-ray spectromicroscopy using ptychography with randomly phased illumination. *Nat. Commun.* **4**, 1669 (2013).

3

7. Jones, M. W. M. *et al.* Whole-cell phase contrast imaging at the nanoscale using Fresnel Coherent Diffractive Imaging Tomography. *Sci. Rep.* **3**, 2288, doi:10.1038/srep02288 (2013).

8. Nam, D. *et al.* Imaging Fully Hydrated Whole Cells by Coherent X-ray Diffraction Microscopy. *Phys. Rev. Lett.* **110**, 098103 (2013).

9. Nugent, K. A. Coherent methods in the X-ray sciences. *Adv. Phys.* **59**, 1–99 (2010).

10. Rodenburg, J. M. *et al.* Hard X-ray lensless imaging of extended objects. *Phys. Rev. Lett.* **98**, 034801 (2007).

11. Putkunz, C. T. *et al.* Phase-Diverse Coherent Diffractive Imaging: High Sensitivity with Low Dose. *Phys. Rev. Lett.* **106**, 013903 (2011).

12. Jones, M. W. M. *et al.* Rapid, low dose X-ray diffractive imaging of the malaria parasite *Plasmodium falciparum*. *Ultramicroscopy* **143**, 88–92 (2014).

13. Godden, T. M., Suman, R., Humphry, M. J., Rodenburg, J. M. & Maiden, A. M. Ptychographic microscope for three-dimensional imaging. *Opt. Express* **22**, 12513–12523 (2014).

14. Faulkner, H. M. L. & Rodenburg, J. M. Movable aperture lensless transmission microcroscopy: a novel phase retrieval algorithm. *Phys. Rev. Lett.* **93**, 023903 (2004).

15. Humphry, M. J., Kraus, B., Hurst, A. C., Maiden, A. M. & Rodenburg, J. M. Ptychographic electron microscopy using high-angle dark-field scattering for sub-nanometre resolution imaging. *Nat. Commun.* **3**, 730 (2012).

16. Kaulich, B., Thibault, P., Gianoncelli, A. & Kiskinova, M. Transmission and emission x-ray microscopy: operation modes, contrast mechanisms and applications. *J. Phys.: Condens. Mat.* **23**, 083002 (2011).

17. Clark, J. N. *et al.* Quantitative phase measurement in coherent diffraction imaging. *Opt. Express* **16**, 3342–3348 (2008).

18. Kim, C. *et al.* Fresnel coherent diffractive imaging of elemental distributions in nanoscale binary compounds. *Opt. Express* **22**, 5528–5535 (2014).

19. Jones, M. W. M., Peele, A. G. & van Riessen, G. A. Application of a complex constraint for a complex sample in coherent diffractive imaging. *Opt. Express* **21**, 30275–30281 (2013).

20. Kirz, J., Jacobsen, C. & Howells, M. R. Soft X-ray microscopes and their biological applications. *Q. Rev. Biophys.* **28**, 33–130 (1995).

21. Howells, M. R. *et al.* An assessment of the resolution limitation due to radiation-damage in X-ray diffraction microscopy. *J. Electron Spectrosc.* **170**, 4–12 (2009).

22. van Riessen, G. A., Junker, M., Phillips, N. W. & Peele, A. G. A soft X-ray beamline for quantitative nanotomography using ptychography. *Proc. SPIE* **8851**, 885117 (2013).

23. Vine, D. J. *et al.* An in-vacuum x-ray diffraction microscope for use in the 0.7-2.9 keV range. *Rev. Sci. Instrum.* **83**, 033703 (2012).

24. Benavente, J. J. M., Mogami, H., Sakurai, T. & Kazuaki, S. Evaluation of silicon nitride as a substrate for culture of PC12 cells: an interfacial model for functional studies in neurons. *PloS ONE* **9**, e90189 (2014).

25. Friedman, J. R. *et al.* ER tubules mark sites of mitochondrial division. *Science* **334**, 385–362 (2011).

26. Koutsopoulos, O. S. *et al.* Human Miltons associate with mitochondria and induce microtuble-dependent remodeling of mitochondrial networks. *Biochim. biophys. acta* **1803** (2010).

27. Williams, G. J., Quiney, H. M., Peele, A. G. & Nugent, K. A. Fresnel coherent diffractive imaging: treatment and analysis of data. *New J. Phys.* **12**, 035020 (2010).

Acknowledgments

Author contributions

M.W.M.J., K.E., M.B.L. and G.A.v.R. designed and undertook the experiment. M.W.M.J., K.E., M.D.J., M.T.R., A.G.P. and G.A.v.R. analyzed and interpreted the results. K.E. prepared the samples, and all authors wrote the manuscript.

Additional information